ADVANCED MATERIALS TECHNOLOGIES
www.advmattechnol.de

Magnetic Actuator with Programmable Force Distribution and Self-Sensing for Bidirectional Deformation Control

Yinduan Gao, Huaxia Deng, Jingyi Zhang, Quan Shu, Zhenbang Xu, Xufeng Cao, Bochao Wang, and Xinglong Gong**

The realization of bidirectional deformation function is an important symbol of most natural creatures and intelligent flexible robots. Currently, most soft actuators are developed on the basis of transition between two different states, which means difficulties of control during the whole movement. In this work, variable distribution positions of hard magnetorheological elastomers (H-MREs) in the matrix are used to achieve different magnetic force distributions. The programmable force distribution promotes different deformations of the magnetic actuators, which enlarges the deformation range by 51.69% under the same magnetic field. Pre-magnetizing the H-MREs makes them have a certain residual magnetization. Due to the residual magnetization property of H-MREs, the magnetized actuator can not only be attracted but also be repelled by the applied magnetic field. This bidirectional deformation capability gives the actuators a wider deformation range and greater clamping force, such as the smart gripper for pinching up object. In addition, the actuators are integrated with a flexible sensing layer with high resolution and strong stability for self-sensing. This kind of force distribution programmable technology and self-sensing performance have the potential to broaden the application of actuators in medical equipment requiring high control accuracy.

1. Introduction

Bidirectional deformation is critical for the realization of specific locomotor functions of most natural creatures, such as the swing of the birds' wings and fishes' tails.[1,2] This kind of movement can be realized through the design of a mechanical structure,[3] but the mechanical structure has high rigidity and limited freedom, which limit its application to bionic actuators.[4,5] Thus, various types of soft actuators have been developed to realize bidirectional deformation. Currently, most soft actuators, for example, shape memory material[6–8] and liquid metal,[9–11] are developed on the basis of transition between two different states, which complicate the control of overall movement. However, in order to realize more precise bionic movement, the whole process of bidirectional deformation can be controlled to achieve better actuating speed and body control, which is still a challenge for the development of soft actuators.

The current actuating principles of soft actuators can be mainly summarized into three categories.[12] The first type is based on the principle of phase transition. The deformation function is realized by the change of the microstructure and macroscopic state of the material under external stimuli.[13] The reciprocal transition of materials between solid, liquid, and gaseous phases is the most prevalent phase change occurrence. The intermolecular interaction between the components causes the entire material to undergo a sequence of property changes or deformations during the phase change process.[14,15] The second type is based on the strain mismatch of different components of the composite structural system.[16] Subjected to the external excitation, the uncoordinated strain between the components creates internal stress at the interface, which in turn lead to the structure's reaction, such as bending deformation,[17] due to the varying mechanical characteristics of each part. The third type is based on the principle of mechanical instability,[18,19] which includes both microscopic and macroscopic structural instability levels. At the microstructural level, the material is considered to be a composite composed of many phases. Instability is manifested as a rapid transition to a position of low potential energy by skipping uniform changes between different phases of the material. At the macroscopic structure level, mechanical instability is usually manifested as buckling, torsion, wrinkling, and so on.[20–24] These large deformations lead to the mode conversion of the structure. The above soft actuators are difficult to control through the whole process of bidirectional deformation since the discontinuity of the switching between the two states.

The magnetic actuator is not limited to switching between the two states.[25,26] It can be continuously controlled by the action of magnetic particles through the magnetic field. The

Y. Gao, H. Deng, J. Zhang, Q. Shu, X. Cao, B. Wang, X. Gong
CAS Key Laboratory of Mechanical Behavior and Design of Materials
Department of Modern Mechanics
University of Science and Technology of China
Hefei 230027, P. R. China
E-mail: hxdeng@ustc.edu.cn; gongxl@ustc.edu.cn
Z. Xu
CAS Key Laboratory of On-Orbit Manufacturing and Integration for Space Optics System
Changchun Institute of Optics
Fine Mechanics and Physics
Chinese Academy of Sciences
Changchun 130033, P. R. China

The ORCID identification number(s) for the author(s) of this article can be found under https://doi.org/10.1002/admt.202200047.

DOI: 10.1002/admt.202200047

magnetic actuators can be divided into soft magnetic actuators[27,28] and hard magnetic actuators[29–31] according to the different types of magnetic particles in the actuator. For soft magnetic actuators, the particles, normally in chain structures,[32,33] are attracted by external magnetic field to achieve actuating ability. The residual magnetization of soft magnetic particles is very small, which has the benefit of repeatability but is difficult for bidirectional movement control. Different from soft magnetic actuators, the magnetized particles themselves has a certain degree of magnetization for hard magnetic particles, even in the absence of a magnetic field.[34] Furthermore, with a tiny magnetic field, the magnetization shift in the hard magnetic elastomer material is quite minimal and can be ignored.[35] This kind of residual magnetization enables the hard magnetic elastomer to achieve not only the attraction from the magnetic field but also the repulsion. As a result, hard magnetic actuators have bidirectional deformation capabilities. The control of hard magnetic actuators has two aspects: open-loop control and feedback control. For open-loop control, the movement is controlled by the predesigned magnetic field on the basis of theoretical modeling prediction. For example, a working environment for the magnetic soft continuum robot (MSCR) that worked in blood arteries was developed on the basis of integrated theoretical modeling and genetic algorithms.[36] A complex magnetic field generating device, BigMag,[37] was developed for the magnetically actuated robot. In order to achieve straight travel and freely turn, BigMag decoupled the two functions of mobility and grasping by adjusting the frequency and direction of the actuating magnetic field. In open-loop control, the movement of the magnetic actuators is predesigned and very difficult to change according to different working conditions. Thus, in feedback control, normally with strain sensors,[28,38–40] the magnetic actuator is controlled according to the motion detection and control target. Since the magnetic actuator works in a magnetic field environment, some researchers also use magnetic field sensors for signal acquisition.[29,41] The use of this kind of sensing element is an essential step for the intelligent and integrated application of magnetic actuators in robots.[42–45] However, with the increasing complexity of the application environment, it is difficult to meet the control requirements only by a single factor. By combining the above two control methods, not only fast open-loop control but also feedback information can be obtained. The deformability of the actuator directly depends on the force field distribution on its torso. It is hard to obtain the controllability of the force field distribution at any position only through the adjustment of the magnetic field. The design of the material distribution is obviously the most effective way. This method can program the position of force distribution, so as to achieve the controllable deformation of the whole field.

In this work, we designed different distribution types of H-MREs in the soft material matrix to achieve the purpose of programming force distribution. The obtained magnetic actuators produced different magnitudes of deformation under a gradient magnetic field, which proved that this control method could not only produce bidirectional deformation but also improve the control ability of the magnetic actuator under a magnetic field, and the silver nanowire (AgNW) sensing layer was fabricated by a spin coating method and mask method. This flexible sensing layer could be perfectly combined with the magnetic actuator, as well as had the characteristics of high resolution, strong stability, and large deformation detection. Through different experimental platforms, the mechanical behavior, magnetic behavior, and sensing behavior of the magnetic actuator have been comprehensively studied. Then, we used the finite element software COMSOL Multiphysics to simulate the actuating behavior of the magnetic actuator. The simulation results again verified that the control ability can be improved by programming the force distribution, and explained the working mechanism of the AgNW sensing layer. Finally, the application capability of this magnetic actuator was demonstrated through the smart gripper experiment and the sequential brake experiment.

2. Results and Discussion

2.1. Fabrication and Structural Characterization

The sample fabrication is depicted in **Figure 1**a, which can be divided into two major steps. The first step was the fabrication of distributed H-MREs using the mold made by a fused deposition printer (Creator-pro, FlashForge Technology Co., Ltd., China), and the second step was to construct the AgNW conductive layer using spin coating method and mask method. In the first step, the polydimethylsiloxane (PDMS) prepolymer, curing agent (weight ratio: 15:1), and neodymium iron boron particles (NdFeBs, 50 wt%) were mixed and stirred for 10 min before being transferred to mold-1. The plane size is shown in Figure S1, Supporting Information, while the thickness was 0.8 mm. The mixture was then degassed for 10 min in a vacuum container and cured for 20 min at 80 °C. The cured intermediate product was transferred to mold-2 (60 × 16 × 2 mm) and poured with PDMS (weight ratio: 15:1). Eventually, the distributed H-MREs were obtained after being degassed for 10 min in a vacuum container and cured at 80 °C for 20 min. In the second step, PDMS (with the same proportion as above) was poured on the silicon wafer, pre-spin-coated at 500 rpm for 15 s, then at 1000 rpm for 30 s, and cured at 80 °C for 20 min. Then, the mask which was made by laser cutting polyethylene film (for dimensions, see Figure S2, Supporting Information) was attached on top of the cured PDMS film. The path was coated with 0.5 mL AgNW solution (7.24 mg mL^{-1}) and dried in air for 10 min. This process was repeated three times to form conductive networks of AgNWs. The polyethylene film (PET film) was then separated from the PDMS film. The electrodes were subsequently made using wires and silver paste. In order to prevent the conductive layer from being damaged, a PDMS film was created in the same way. Then, a 60 mm × 16 mm conductive layer was obtained by cutting. Finally, PDMS was spin-coated onto the distributed H-MREs; the conductive layer was adhered to them, and they were cured at 80 °C for 20 min. The sample was placed in a magnetic field generator and magnetized with a uniform magnetic field of 1.5 T flux density for 10 min. Figure 1b shows the internal H-MREs distribution of the three samples. By programming the material distribution, the length of each section from the free end to the fixed end

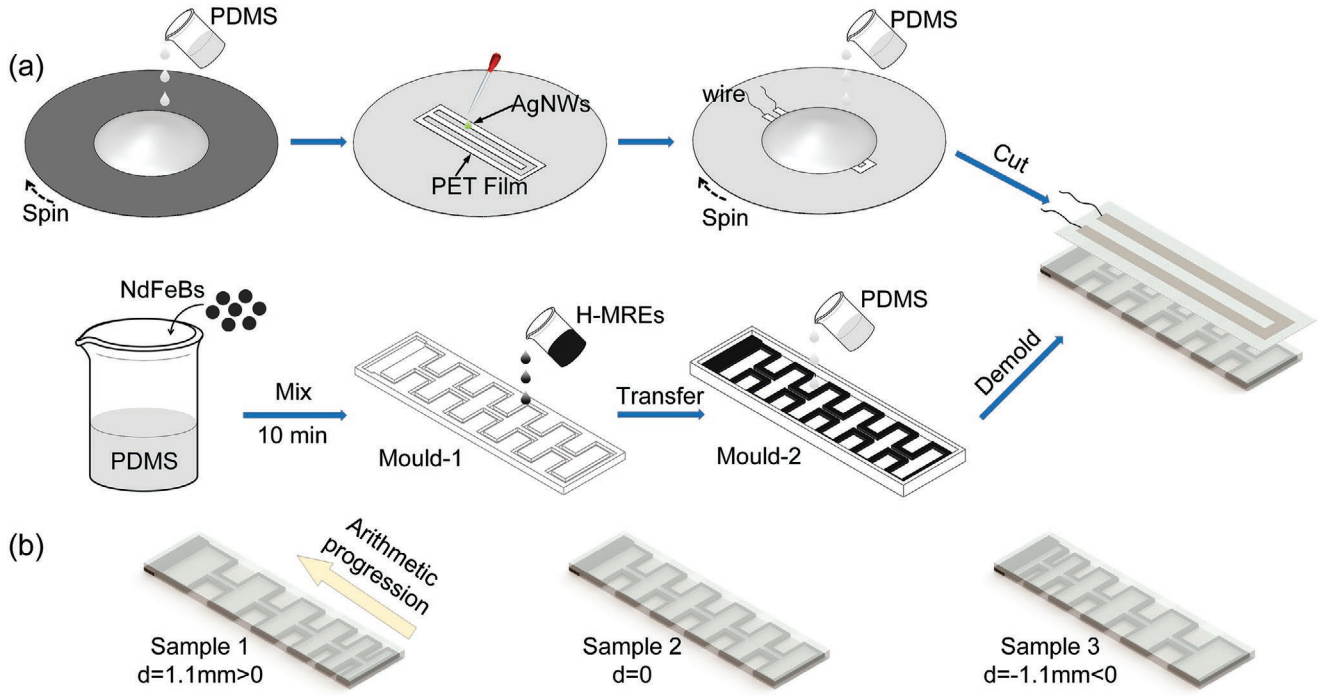

Figure 1. Sample preparation. a) The experimental process of sample preparation. b) Schematic diagram of different samples.

can form an arithmetic progression. The common difference "d" of samples 1, 2, and 3 is 1.1 mm, 0, and −1.1 mm, respectively. In the samples without electrical experiments, the steps for fabricating AgNWs conductive layer were omitted except for other steps.

The composition and morphology of the microstructure determined the macroscopic properties of materials. First, the internal structure of the sample was characterized by scanning electron microscope (SEM). The SEM image (**Figure 2**a) showed a cross-sectional view of the conductive sample, which contained a multilayer structure. The PDMS protective layer was at the top, followed by the AgNW layer, PDMS layer, and H-MRE layer. A magnified observation of the AgNW layer, as shown in Figure 2b, showed that the thickness of the

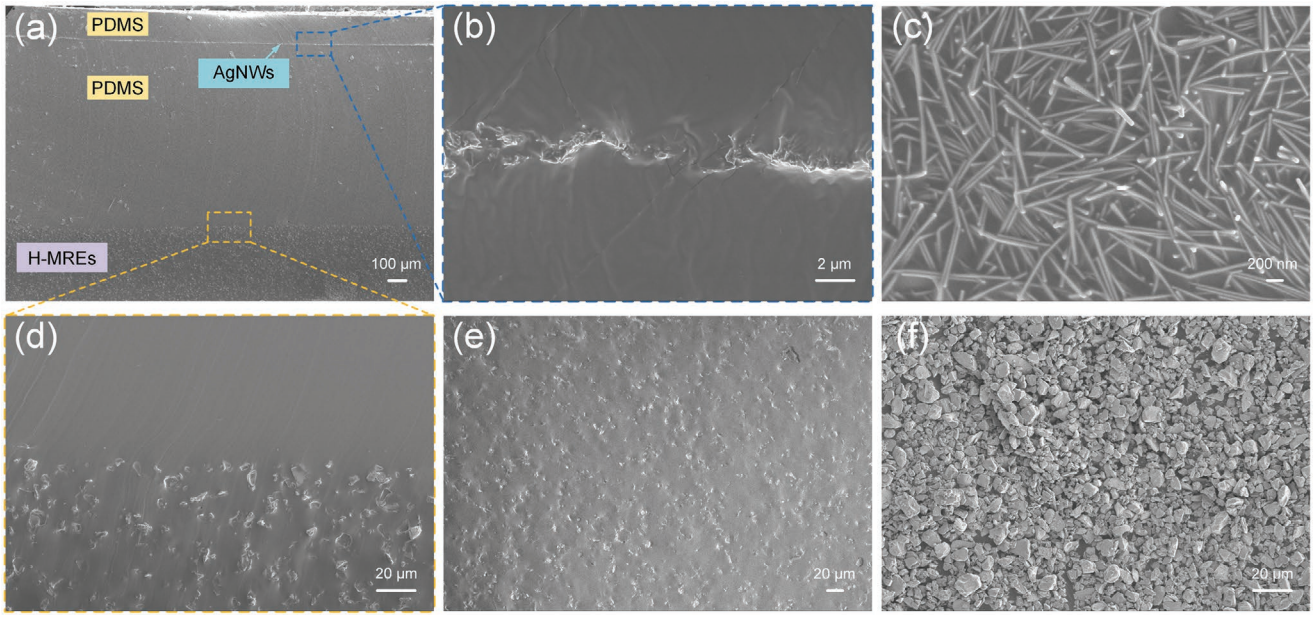

Figure 2. Microstructure characterization of samples. a) Conductive sample profile. b) Enlarged view of AgNW layer. c) Top view of AgNW layer. d) Enlarged view of the H-MREs and PDMS bonding layer. e) Particle distribution in the H-MREs. f) SEM image of the NdFeBs.

AgNW layer was very thin, less than 1 µm. Figure 2c depicts a top view of the AgNW layer. Any single AgNW had an elongated shape with comparable size, indicating the consistency of the fabrication. It can also be seen that all of the AgNWs were interlaced to form a dense network structure, which provided stable conductivity of the sample. Figure 2d shows that there were no obvious defects at the junction of layers, which indicate that two layers of PDMS can be well combined, and also proved the feasibility of this layered manufacturing technology. Figure 2e shows that the NdFeBs particles were entirely embedded in the matrix and were uniformly dispersed throughout. In addition, no bubbles were generated in the matrix. The last image showed that the size of the NdFeBs was slightly different.

2.2. Programmed Bending Angles

The magnetic behavior of magnetic materials depended directly on the morphology of hysteresis loops. Therefore, before conducting magnetic response studies, the hysteresis loops of NdFeBs and H-MREs were tested. As shown in Figure S3, Supporting Information, the highest magnetic field strength during testing was 1200 kA m^{-1}. It can be seen from the figure that the material had great residual magnetization and coercivity. The hysteresis loop was full in shape, which was a typical hard magnetic characteristic. The saturation magnetization of NdFeBs was 0.1354 $A \cdot m^2 g^{-1}$, the residual magnetization was 0.0968 $A \cdot m^2 g^{-1}$, and the coercivity was 400.7 kA m^{-1}, while for H-MREs was 0.0676 $A \cdot m^2 g^{-1}$, 0.0452 $A \cdot m^2 g^{-1}$, and 475.7 kA m^{-1}, respectively. The saturation magnetization and residual magnetization of NdFeBs were about twice that of H-MREs, which was closely related to the mass fraction of NdFeBs in H-MREs. The reason for their different coercivity was that the magnetic particles inside the H-MREs were almost completely fixed, while a small fraction of the NdFeBs may rotate when tested. Therefore, the coercivity of the NdFeBs was slightly smaller.

In addition, to verify the feasibility of this programming force distribution method, the deformation characteristics of different samples under magnetic fields were tested. The test device diagram is shown in **Figure 3**a. The sample was fixed 50 mm away from the electromagnet. The electromagnet generated a space magnetic field by using a DC power supply. The magnetic field generated by the electromagnet was positive to the right, and the bending angles (the angle between the vertical direction and the free end of the samples) of the samples were positive to the counterclockwise. In Figure 3, the magnetic flux density measurement point was the initial position of the sample, and the direction was perpendicular to the electromagnet. The magnetic flux density distribution of the electromagnet is shown in Figure S4, Supporting Information. According to Figure 3b, as the magnetic flux density increased, the bending angles of the three samples increased approximately linearly. In the results, the largest bending angles were sample 1, followed by sample 2 and sample 3. The bending angles of sample 2 were close to that of sample 3, which was also reflected in the subsequent simulation. The

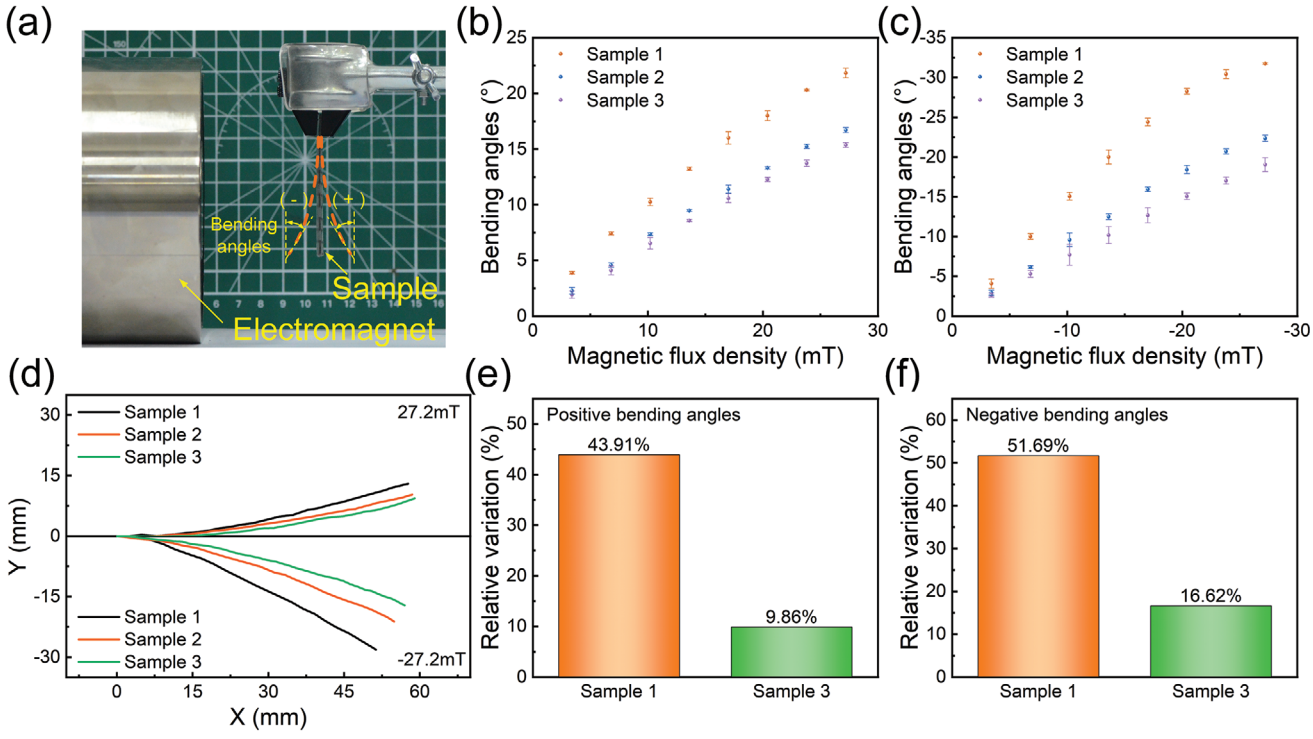

Figure 3. Magnetic response of samples. a) Schematic diagram of sample deformation testing system under magnetic field. b,c) Bending angles of three samples under different magnetic flux density. d) The deformed shape of the samples under the ±27.2 mT magnetic flux density. e,f) The relative variation of other samples relative to Sample 2 under positive and negative bending.

main reason was that the force acting on the free end of the cantilever beam could cause greater bending deformation than the force acting on the middle or fixed end of the cantilever beam, and sample 1 distributed more H-MREs at the free end, resulting in greater magnetic force at this end. In Figure 3c, as the magnetic field reversed, the bending direction of the samples also reversed. At the same time, it can be found that the relationship between the bending angles of sample 1 and the magnetic flux density was not a simple linear relationship, but a linear relationship when the bending angles were small. When the bending angles reached a certain value, the curve was close to the saturation relationship. The main reason was that the bending of the sample was the result of the combined action of magnetic field force, elastic restoring force, and gravity. After the bending angles increased to a certain extent, the elastic restoring force increased sharply. The error bars in Figure 3b,c show the standard deviation of sample deformation under multiple tests. There was little difference between the test results of multiple experiments, which was because hard magnetic materials had stable magnetic properties under small magnetic fields. Figure 3d shows the deformed shapes of the three samples under the maximum positive and negative magnetic field, which can clearly show the difference in the deformation of the three samples. The same sample deformed more at negative magnetic flux density due to the asymmetry of the gradient field. It can be seen in Figure S4, Supporting Information, that there was a larger flux density and gradient near the electromagnet. Then, the average value of the relative variation in bending angles with respect to sample 2 was calculated based on the data in Figure 3b,c. It can be seen that the relative variation of sample 1 was higher than sample 3. The relative changes of sample 1 in the two directions reached 43.91% and 51.69% respectively, which meant that the deformation range of the magnetic actuator was significantly changed by force distribution programming. Overall, this method of improving the control ability of magnetic field on magnetic soft material was effective.

2.3. Self-Sensing Performance

Self-sensing was important for movement control. As the sensing layer shape of these samples remained consistent, only conductive samples with the same internal structure as sample 2 were used for the study. It could sense its own actuating state, which was very important for improving the control ability of the actuator. This section used a series of experimental systems to characterize the self-sensing performance of the conductive samples. First, the sensing properties of conductive sample were studied under mechanical bending load. Considering that the actuator would be stretched when grabbing and lifting heavy objects, the sample was subjected to tensile tests under DMA. Finally, the effect of magnetic field on the sensing performance of the sample was investigated.

As shown in **Figure 4**a, it was a test system with a sample under mechanical loading, including a reciprocating drive, a hertz regulator, and a displacement adjuster. The signals were obtained through the Modulab material testing system. In the experiment, the displacements were loaded by the reciprocating drive and the displacement adjuster, and the hertz regulator was used to adjust the frequency. First, as shown in Figure 4b,c, the effect of loading displacements on resistance change was tested in actuating direction 1. The minimum loading displacements were 1.5 mm, and the maximum loading displacements were 12 mm. It can be seen from the figure that the normalized relative resistance change $\Delta R/R$ (where R was the initial value of resistance, and ΔR was the amount of resistance change) was a negative value. As the loading displacements increased, the absolute value of $\Delta R/R$ also increased. As shown in Figure 4d,e, when loading in direction 2, $\Delta R/R$ was positive, and at the same loading displacements, the absolute value of $\Delta R/R$ in direction 1 was larger. Under each loading displacement, the relative resistance change data under ten loading cycles was given, and the ten groups of data had little fluctuation. In Figure 4f,g, the resistance change characteristics of different loading frequencies in two directions are shown. It can be seen that within a certain range, the loading frequency had almost no effect on the resistance change. In Figure 4h,i, the real-time detection of the resistance change when loading and unloading in direction 1 and direction 2 is given, which shows the stability of the soft conductive layer under the mechanical-electric response.

The mechanical and electrical properties of the conductive sample during stretching were tested by the DMA test device. The device diagram is shown in **Figure 5**a. The conductive sample was fixed with the DMA clamps and the length of the conductive sample in the stretching section was 40 mm. As the tensile strain increased, $\Delta R/R$ also kept increasing, from 9.30% under 2% tensile strain to 108.71% under 16% tensile strain (Figure 5b). Figure 5c is an enlarged view at 10% tensile strain in which it can be seen that the repeatability and recovery of resistance were acceptable. Simultaneously, the connection between force sensing and tensile strain was recorded, and the sample's stress and strain were calculated (Figure 5d–f). It can be seen from the stress–strain relationship graph that the material had elastic properties, and there was almost no hysteresis effect. Then, the resistance and force response of the conductive sample at different stretching frequencies were studied (Figure 5g). It can be seen from the figure that the $\Delta R/R$ and force of the conductive sample remained stable at 0.125, 0.25, 0.5, and 1 Hz, respectively. The results showed that the sensing performance and mechanical properties of the conductive sample were hardly affected by the stretching frequency, which were similar to the results of the mechanical bending loading experiment. Subsequently, the sensitivity coefficient of the conductive sample sensing performance was calibrated (Figure 5h). Here, the sensitivity coefficient GF_t is expressed as $(\Delta R/R)/\varepsilon_t$, $\varepsilon_t = \Delta l/l_0$, where ε_t refers to the tensile strain of the conductive sample, and Δl and l_0 are the length change and the initial length of the conductive sample. Through fitting, the sensitivity coefficient of the conductive sample under tensile strain was 7.20 ± 0.09, and the fitting coefficient was 0.998, indicating a linear relationship between $\Delta R/R$ and tensile strain. Finally, a square wave with a tensile strain of 10% was used to evaluate the transient response behavior of the conductive sample. When the DMA clamp suddenly raised by 4 mm, both the $\Delta R/R$ and the force experienced a sudden increase and exceeded the

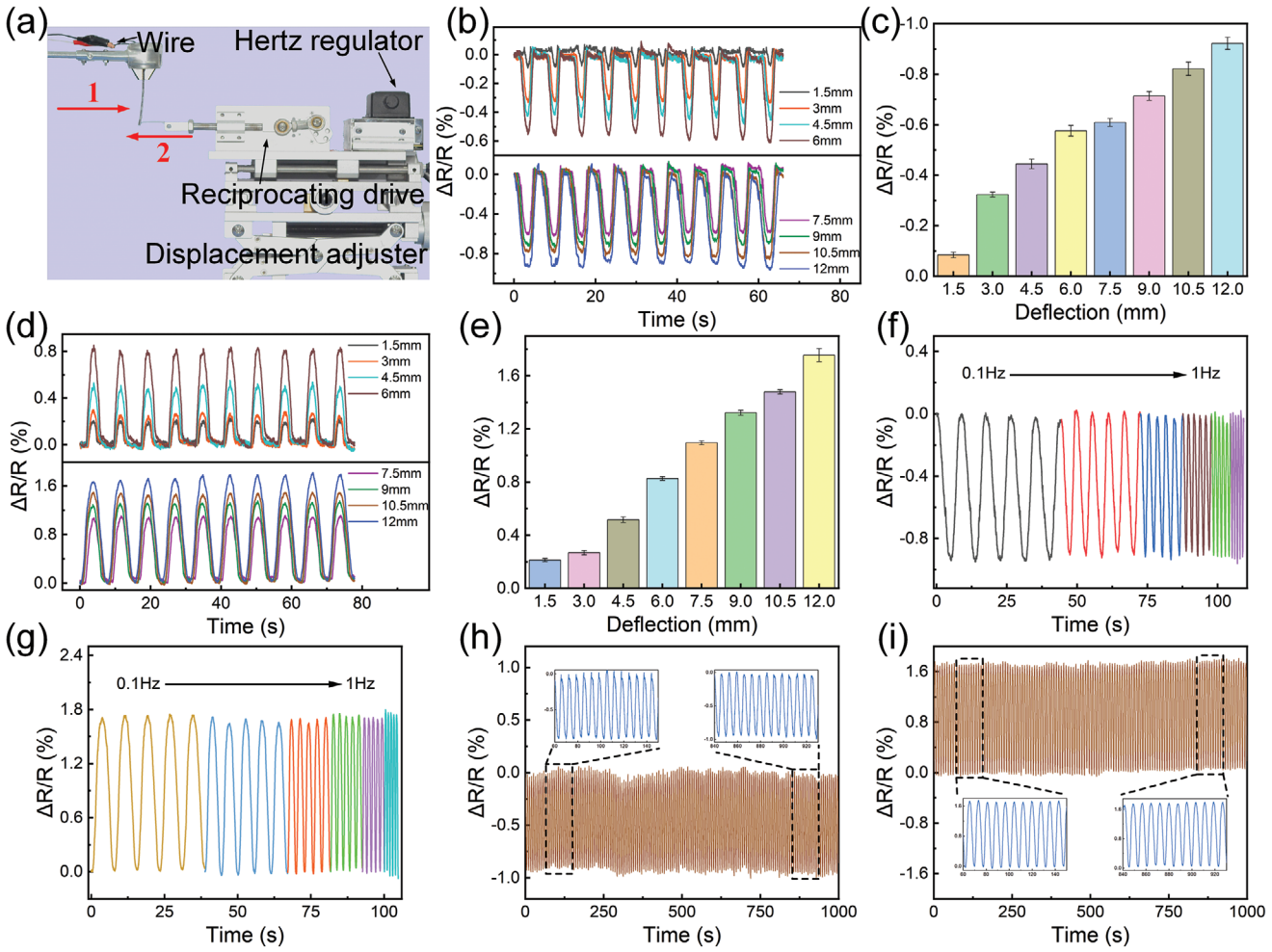

Figure 4. Resistance change under mechanical loading. a) Schematic diagram of measurement system. b–e) Diagram of relative resistance change at different loading distances in direction 1 or direction 2. f,g) The effect of loading frequency. h,i) Stability test under cyclic loading.

stable value, and then slowly returned to the stable value. In the unloading stage, $\Delta R/R$ recovered slowly, but the force had a sharp point, which was caused by the inertia effect that was difficult to ignore during the loading and unloading process of the square wave.

In order to study the electrical properties of the conductive sample more deeply, the electrical response experiment of the conductive sample under the action of a magnetic field was carried out. The experimental device is shown in **Figure 6**a. The electromagnet actuated the sample to bend; then the resistance of the conductive sample changed accordingly. The DC power supply was controlled by a computer to produce a half-sine-changing current. Therefore, the electromagnet could generate a half-sine-changing magnetic field. As shown in Figure 6b, the sample was bent to the left under the action of the magnetic field, so the AgNW conductive layer was compressed, and the relative resistance change $\Delta R/R$ was less than 0. Under the lowest test magnetic flux density of 4.3 mT, the resistance also had a certain change, which showed that the AgNW conductive layer had a high resolution. As the magnetic field kept growing, the bending angles of the sample increased, causing the absolute value of $\Delta R/R$ to rise. The direction of the current was then reversed, as shown in Figure 6c, as was the direction of the magnetic field. The magnetic field produced by the electromagnet exerted a repulsive force on the conductive sample, forcing it to bend to the right, and pulling the conductive layer of the AgNWs such that $\Delta R/R$ was positive. As shown above, under the same magnetic flux density, the sample would produce greater bending deformation when it was attracted (Figure 6b). However, comparing Figure 6b,c, the resistance change was more obvious when the AgNWs conductive layer was stretched (Figure 6c). Therefore, in the deformation of the same magnetic flux density in both directions, a larger bending amount did not correspond to a larger resistance change. The resistance change of the sensing layer was more obvious when it was stretched. Figure 6d,e corresponds to the resistance stability test under attraction and repulsion, respectively. For a clearer observation, the magnified data around 950 or 400 s were given. They were slightly worse than the stability data under mechanical bending loading. The main reason may be that the electromagnet was used for a long time with a large current, and the internal resistance of the electromagnet

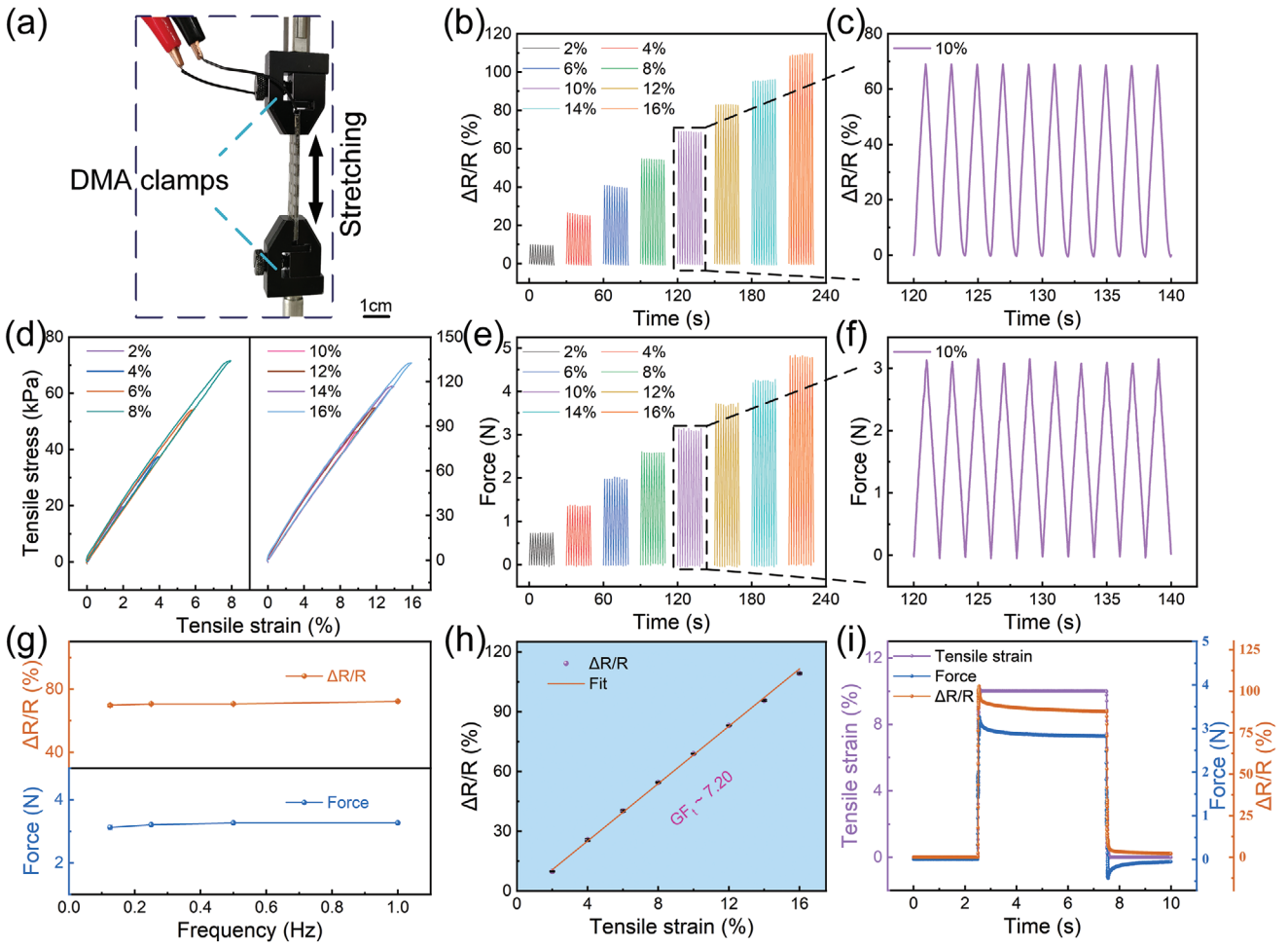

Figure 5. Sample tensile properties. a) DMA tensile testing system image. b,c) $\Delta R/R$ of conductive sample under 0.5 Hz tensile frequency and different tensile strains. d–f) Stress–strain relationship and force change of conductive sample under 0.5 Hz tensile frequency and different tensile strains. g) $\Delta R/R$ and force response to frequency of the conductive sample under 10% tensile strain. h) Relationship between $\Delta R/R$ and tensile strain. i) The force and electrical transient response of the conductive sample under 10% square wave tensile strain.

increased after heating. Finally, a real-time detection diagram of the sample's resistance under square wave current and a magnetic flux density size of 17.0 mT was given. In the attraction curve, the AgNW conductive layer was compressed first, and then the compression was released. In the repulsion curve, the AgNW conductive layer was stretched first, and then the tension was released. Considering the release of compression as a reverse stretch, and the release of tension as a reverse compression. Then, as can be seen from the figure, when the AgNW conductive layer was suddenly compressed, the resistance slowly tended to a stable value. When subjected to a sudden stretch, the resistance suddenly increased and exceeded the stable value, and then slowly decreased to a stable value. This phenomenon was related to the separation between the AgNWs under the stretching of the conductive network.

Through the above series of experiments, the stable sensing performance of the AgNW sensor layer was proved. It could respond not only to mechanical stimulation but also to magnetic stimulation, which proved the feasibility of detecting the actuating state.

2.4. Simulation and Mechanisms

In order to further study and verify the influence of programmed magnetic force distribution on actuators control and the mechanism of AgNWs conductive layer, simulations were carried out through the finite element simulation software COMSOL Multiphysics. First, a uniaxial tensile test was performed on the H-MREs and PDMS by DMA to measure the elastic modulus of the material (Figure S5, Supporting Information). The length of the tensile section was 20 mm, and the cross-sectional dimension was 4 × 2 mm. Only the linear elasticity of the material was considered, so the maximum tensile strain was 15%. The tensile strain rate was set to 4×10^{-3} s^{-1}. Three repeated experiments were carried out for each material. Finally, the three sets of experiments were linearly fitted. The elastic modulus of H-MREs and PDMS were 1190.384 and 675.373 kPa, respectively, and the fitting coefficients were 0.99837 and 0.99969.

In the finite element simulation, the two physical fields of magnetic field (mf) and solid mechanics (solid) were used

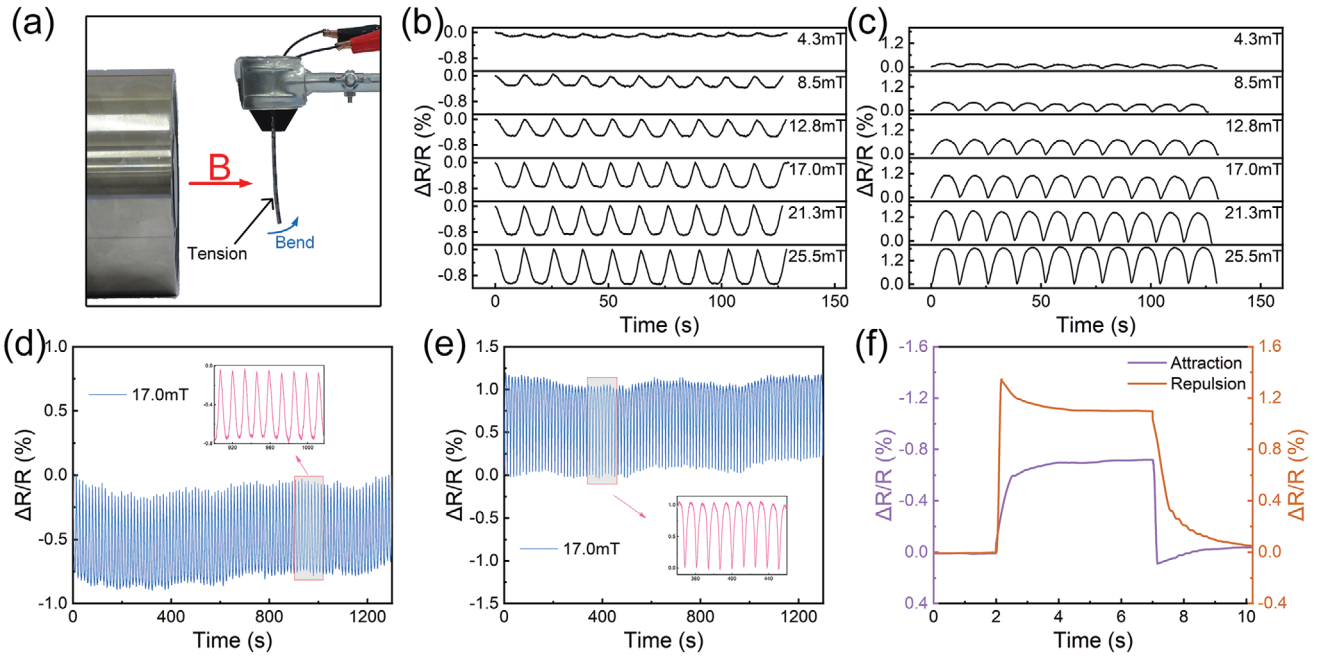

Figure 6. Resistance change under the action of a magnetic field. a) Schematic diagram of measurement system. b,c) Resistance response diagram under different attractive or repulsive magnetic fields. d,e) Resistance cycle test. f) Transient response graph of resistance under square wave magnetic field loading.

for coupling solution, and the study type was a steady-state. Similar to the experimental conditions, the current was set to 3.2 A during the simulation, the samples were fixed 50 mm away from the magnetic field. The samples deformed under the combined action of Maxwell's surface stress tensor and gravity. **Figure 7**a shows the spatial magnetic field generated by the electromagnet. Figure 7b,c shows the strain cloud diagrams of sample 2 along the vertical direction under the action of attraction or repulsion. It can be seen from the figure that under the action of repulsion, the side of the sample facing away from the electromagnet was compressed. Obviously, this corresponded to a decrease in the resistance of the AgNW conductive layer. Similarly, under the action of attraction, the side of the sample away from the electromagnet was stretched, and the corresponding resistance increased. In order to explain the reasons for resistance changes during compression and tension of the AgNW sensing layer, Figure 7d shows the mechanism diagram of internal structure changes. When the sample was compressed, the AgNWs moved closer to each other, increasing the number of contact points, so the resistance became smaller. Similarly, when the sample was stretched, the AgNWs separated from each other, resulting in fewer contact points and therefore higher resistance. Next, the displacement cloud diagrams of the three samples under repulsive action were given. Among them, the maximum displacements of sample 1 were 16.3 mm, while the maximum displacements of sample 2 and sample 3 were 13 and 10.7 mm, respectively. By adjusting the direction of the current in the simulation, the magnetic field distribution was unchanged, but the direction was opposite. The three samples were attracted, and the maximum displacements reached 24.9, 17, and 15.5 mm, respectively (Figure 7h–j). Comparing the repulsion and attraction displacement cloud diagrams of the three samples, it can be found that the displacements of the samples were greater when they were attracted, which was related to the larger magnetic field near the electromagnet. The simulation results agreed well with the experimental results, which once again illustrated the feasibility of this force distribution control method, and also explained the relationship between the AgNWs conductive layer and strain.

2.5. Application Demonstration Experiment

Self-sensing magnetic actuators with programmable force distribution has broad application prospects, such as soft robots and feedback control. In this article, we studied the applications of this multi-function actuator in smart gripper and sequential braking.

In order to achieve versatility for the robot, it was very significant to simulate the process of pinching objects by human hands. For example, the action of pinching was necessary when picking up small objects. As shown in **Figure 8**a, three samples were assembled to prepare the smart gripper. During assembly, the assembly direction of the middle sample was opposite to the other two, so that the object pinching action under the horizontal gradient magnetic field (generated by the permanent magnet) can be realized. Among them, the sample in the middle had sensing performance. When a horizontal rightward gradient magnetic field was applied, the sample in the middle bent to the right, while the samples on both sides bent to the left. At this time, the AgNWs conductive layer was stretched, and $\Delta R/R$ was a positive value. When the direction of the magnetic field was opposite, the deformation

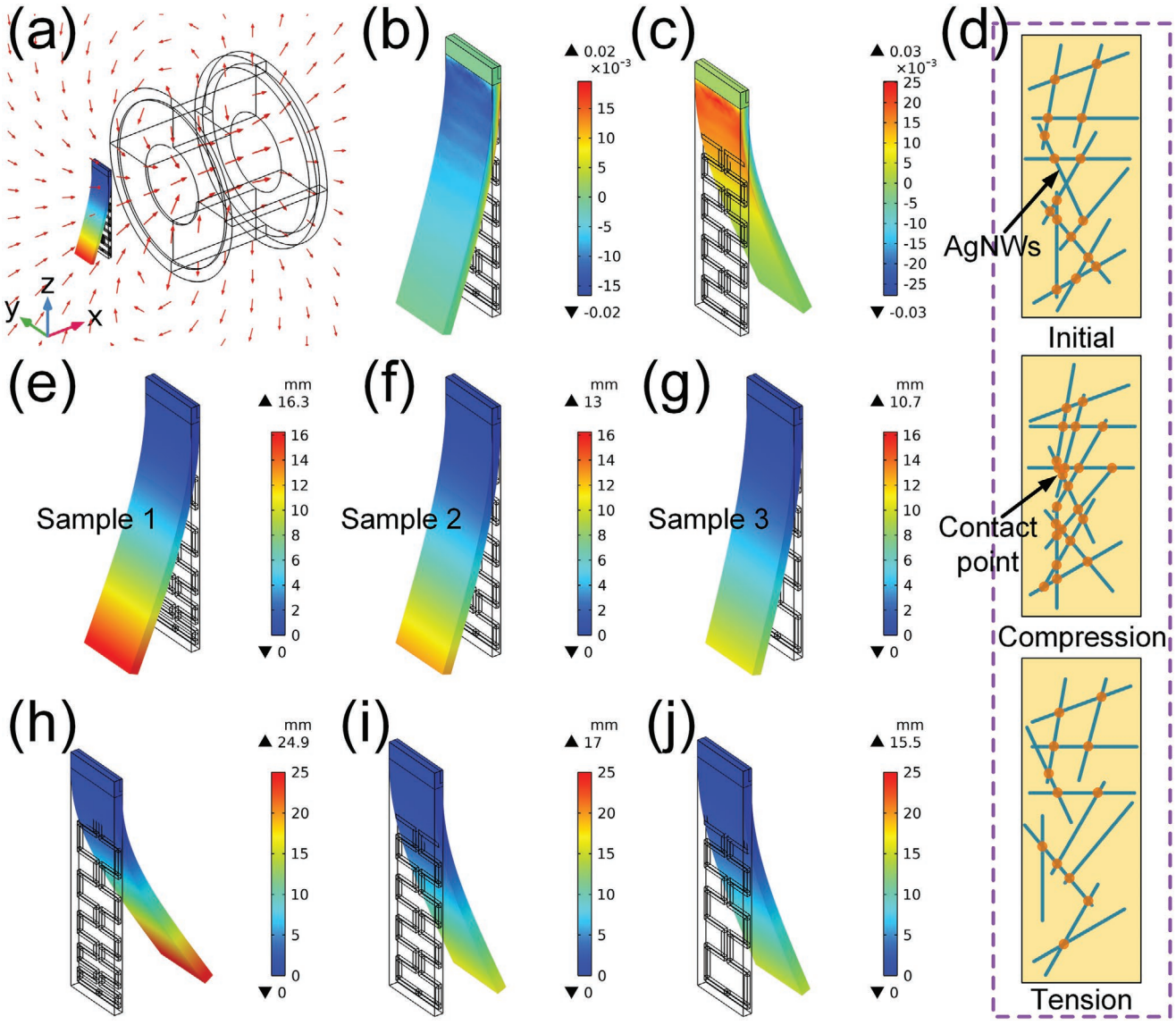

Figure 7. Simulation analysis and mechanism demonstration. a) Distribution diagram of magnetic field generated by electromagnet. b,c) Vertical strain cloud image of sample 2 under the action of repulsion and attraction. d) AgNW resistance changing mechanism demonstration. e–g) Displacement cloud diagram of three samples under repulsion. h–j) Displacement cloud diagram of three samples under attraction.

direction of all samples was also opposite, and $\Delta R/R$ became negative (Figure S6, Supporting Information). Therefore, by applying a magnetic field during operation, the relative resistance changed. When gripping the object, a reverse magnetic field was applied. If the relative resistance change was also reversed, the object was not clamped. If the relative resistance change was not reversed, but the relative resistance change was fixed or reduced, it means that the object was clamped. Pinching an object was a complex process that did not rely just on pulling force, as gripping did, but also on friction. As shown in Figure 8b, under the horizontal rightward magnetic field, the gripper separated and clamped the object, and then the horizontal magnetic field was removed. When the gripper moved upward, the object cannot be picked up due to insufficient friction force (Figure 8c). In order to smoothly pinch the object, a horizontal leftward gradient magnetic field should be applied, which caused the sample to deform in the reverse direction so that clamping the object and increasing the friction force (Figure 8d). Under the horizontal leftward gradient magnetic field, the object was pinched up smoothly (Figure 8e). Then, in Figure 8f,h, the process of putting down the object was simulated. The gripper first moved downward with the object under the horizontal leftward magnetic field. After reaching the designated position, the magnetic field was removed, and the gripper moved upward and left the object. The above experimental process verified that the intelligent gripper could smoothly simulate the process of grasping small objects by human hands. It can be summed up as first turning on the device, placing it where the object was, then applying an opposing force to tighten the object and lift it up.

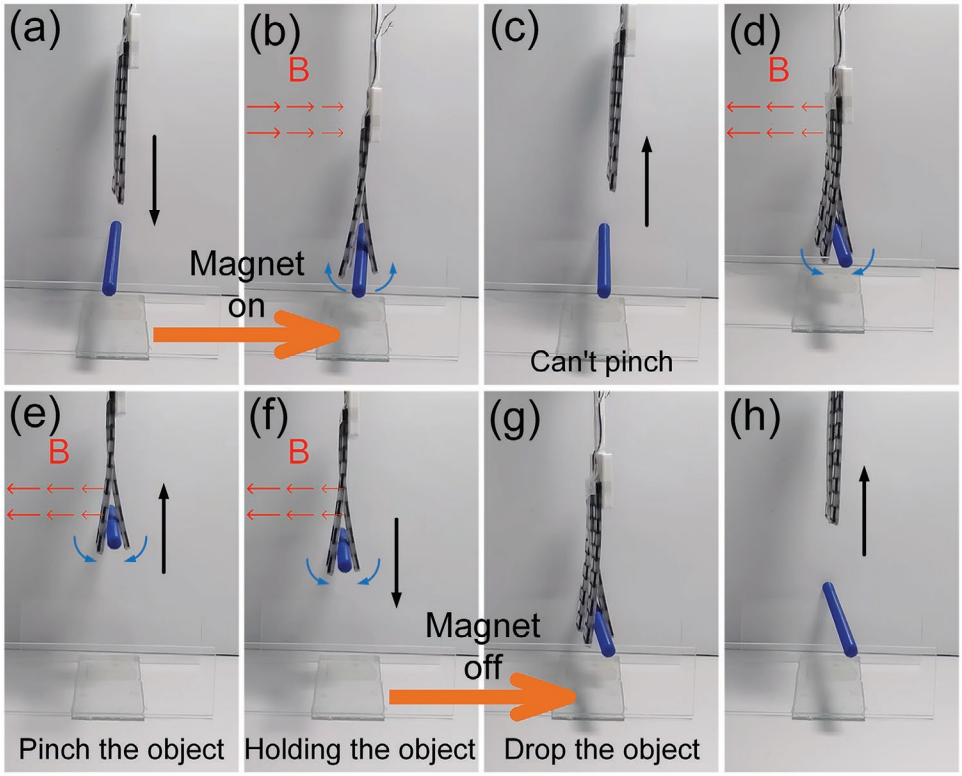

Figure 8. Smart gripper demonstration experiment. a–c) Smart gripper grabbed object without reverse magnetic field. d,e) Smart gripper grabbed object under a reverse magnetic field. f–h) The process of dropping the object by the smart gripper.

This provided the robot gripper with the ability to grip objects, which was beneficial to the development of its multifunctionality. For more detailed experimental procedures, please watch Movie S1, Supporting Information.

A general electromagnetic relay can only control one switch. To realize the control of multiple switches, separate control of multiple magnets is required. It is difficult to implement an electromagnetic relay that controlled multiple switches by a single magnetic field. In this article, a sequence brake was made by the magnetic actuator with a programmable force distribution, which could control multiple switches at the same time by only one magnetic field. **Figure 9**a shows the circuit diagram of the sequential brake. During the production process, the left end of the sample was fixed, and the free end was pasted with a 10 mm × 10 mm copper foil, and the circuit was disconnected at the free end of the sample. At the beginning, under the action of gravity, the sample was tightly attached to the bottom plate. The copper foil at the end was used as a switch to connect the circuit, so the three LEDs all glowed (Figure 9b). Under the action of magnetic field perpendicular to the surface of the paper, with the increase of magnetic flux density, the three switches were opened successively at 3.1, 5.4, and 6.6 mT, and the LEDs went out (Figure 9c–e). Then, the magnetic flux density was reduced. When the repulsive force of the magnetic field was less than the gravity, the switch could be closed again, and the three LEDs could be turned on sequentially (Movie S2, Supporting Information). Through this set of experiments, the function of sequential braking was realized, and the practicality of the programmable force distribution was confirmed. The actuator device with this function can make it easier to control the car gears, fan speed, valve size, and other devices that require incremental control.

3. Conclusion

In summary, we reported a magnetic actuator that programmed the distribution of H-MREs to control the distribution of force. By magnetizing the magnetic actuator, the NdFeBs inside had a certain residual magnetization, which could be attracted or repulsed under the gradient magnetic field generated by the electromagnet or permanent magnet. It had been proved that the magnetic actuator was capable of bidirectional deformation. Samples with different distribution types of hard magnetic materials in the elastomer matrix can produce different deformations. Experiments revealed that this technology can increase the deformation range of a magnetic actuator by 51.69%. The AgNW sensing layer was integrated on the sample by spin coating and masking. Test results under various load conditions indicated that this sensing layer had the characteristics of high resolution and excellent stability, and it could also detect the actuating state of the magnetic actuator. The design concept of this programmable force distribution and the resistance change mechanism of the sensing layer were further verified by the finite element method using magnetic field analysis and deformation analysis. Finally, this kind of magnetic actuator was used for smart gripper and sequential brake demonstration, which proved that it had a broad application platform.

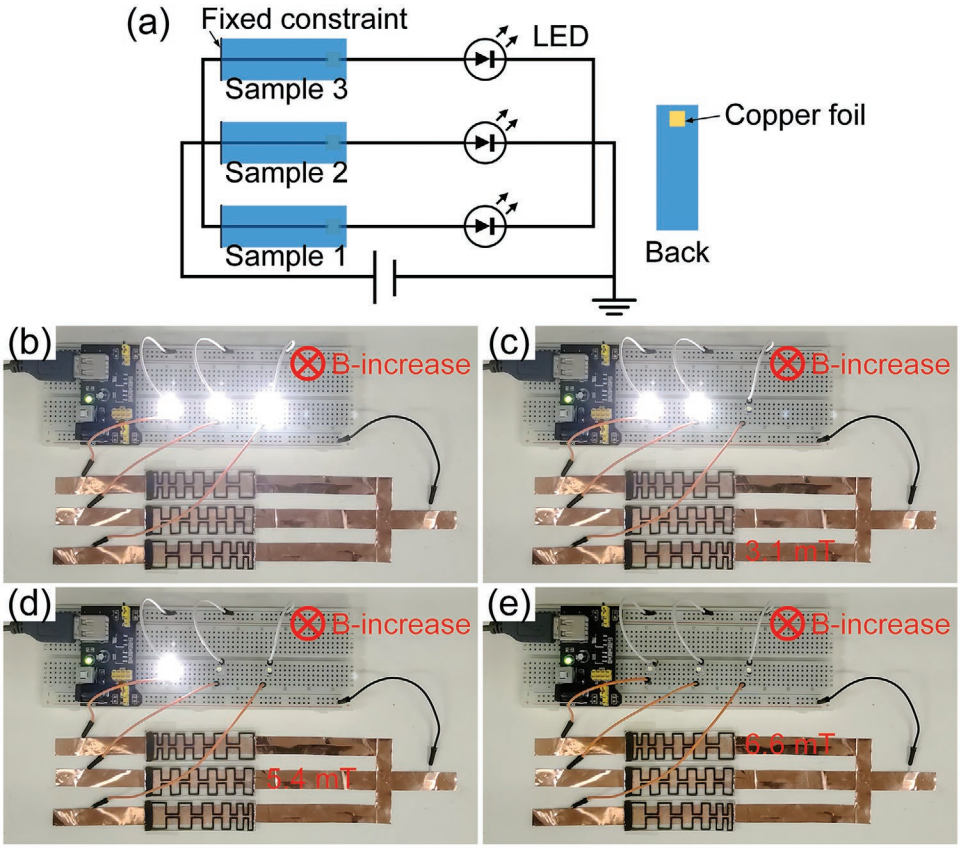

Figure 9. Sequential braking demonstration experiment. a) Circuit diagram. b) The initial state of the device. c–e) The three LEDs (light-emitting diodes) were extinguished one by one under the action of the magnetic field.

4. Experimental Section

Materials: The PDMS prepolymer and curing agent (Sylgard 184) were supplied by Dow Corning GmbH. NdFeBs were purchased from Guangzhou Nord Transmission Co., Ltd., China, with an average particle size of 5 µm. The reagents used to fabricate AgNWs were provided by China Shanghai Sinopharm Chemical Reagent Co., Ltd.

Fabrication of AgNWs: AgNWs were fabricated for self-sensing of material since of electronic conductivity properties. In this article, it was independently synthesized by raw materials of polyvinylpyrrolidone (PVP), glycerol ($C_3H_8O_3$), sodium chloride (NaCl), silver nitrate powder ($AgNO_3$), and deionized water. First, 190 mL $C_3H_8O_3$ and 5.86 g PVP were added sequentially to a 250 mL three-mouth flask. The mixture was heated to 90 °C for 30 min at a stirring speed of 250 rpm. After that, stirring continued while cooling to 50 °C in the air; then, 0.059 g NaCl, 500 µL deionized water, 1.58 g $AgNO_3$, and 10 mL $C_3H_8O_3$ were added sequentially, and the mixture was heated to 210 °C for 25 min. Then, the reaction reagent was poured into the beaker and the precipitation diluted with 200 mL deionized water. This was allowed to sit for a week, and then the supernatant poured off. The precipitate was centrifuged twice with deionized water and anhydrous ethanol. Finally, an ethanol solution containing AgNWs was obtained.

Characterization: The microscopic morphology of the sample was characterized by a SEM (Gemini 500, Carl Zeiss, Jena, Germany). The hysteresis loops of NdFeBs and H-MREs were tested by the hysteresis loop instrument (HyMDC). A dynamic mechanical analyzer (DMA, ElectroForce 3200, TA instruments, Minnesota 55 344 USA) was used to test the tensile properties of the samples. A Modulab material testing system (Solartron analytical, AMETEK advanced measurement technology, Inc., United Kingdom) was used to evaluate the electrical properties of the samples (test voltage: 4 V). In addition, a DC power supply (ITECH IT6724), a commercial electromagnet, and a neodymium iron boron permanent magnet were used to generate a magnetic field, and a Tesla meter (HT20, Shanghai Hengtong Magnetic Technology Co. Ltd, China) was used to measure the magnetic flux density. All experiments were performed at room temperature (25 °C).

Supporting Information

Supporting Information is available from the Wiley Online Library or from the author.

Acknowledgements

Financial supports from the National Natural Science Foundation of China (Grant Nos. 12132016, 11972343), the Fundamental Research Funds for the Central Universities (WK2480000030, WK2480000009), and the Anhui's Key R&D Program of China (202104a05020009) are gratefully acknowledged. This study was also supported by the Collaborative Innovation Center of Suzhou Nano Science and Technology.

Conflict of Interest

The authors declare no conflict of interest.

Data Availability Statement

Research data are not shared.

Keywords

bidirectional deformation, magnetic, programmable force distribution, sensor, soft actuator

Received: January 10, 2022
Revised: March 15, 2022
Published online: April 7, 2022

[1] W. B. Chen, C. H. Xiong, C. L. Liu, P. M. Li, Y. H. Chen, *Soft Rob.* **2019**, *6*, 495.
[2] H. Y. Jiang, L. X. Fan, S. Yan, F. B. Li, H. J. Li, J. G. Tang, *Nanoscale* **2019**, *11*, 2231.
[3] A. Cully, J. Clune, D. Tarapore, J. B. Mouret, *Nature* **2015**, *521*, 503.
[4] Y. Cao, J. Y. Dong, *Soft Matter* **2021**, *17*, 2577.
[5] L. Hines, K. Petersen, G. Z. Lum, M. Sitti, *Adv. Mater.* **2017**, *29*, 1603483.
[6] B. T. Michal, C. A. Jaye, E. J. Spencer, S. J. Rowan, *ACS Macro Lett.* **2013**, *2*, 694.
[7] Q. J. Ze, X. Kuang, S. Wu, J. Wong, S. M. Montgomery, R. D. Zhang, J. M. Kovitz, F. Y. Yang, H. J. Qi, R. K. Zhao, *Adv. Mater.* **2020**, *32*, 8.
[8] Q. Zhao, W. K. Zou, Y. W. Luo, T. Xie, *Sci. Adv.* **2016**, *2*, 7.
[9] C. P. Ambulo, M. J. Ford, K. Searles, C. Majidi, T. H. Ware, *ACS Appl. Mater. Interfaces* **2021**, *13*, 12805.
[10] J. Shu, D. A. Ge, E. L. Wang, H. T. Ren, T. Cole, S. Y. Tang, X. P. Li, X. B. Zhou, R. J. Li, H. Jin, W. H. Li, M. D. Dickey, S. W. Zhang, *Adv. Mater.* **2021**, *33*, 10.
[11] Z. J. Ma, Q. Y. Huang, Q. Xu, Q. N. Zhuang, X. Zhao, Y. H. Yang, H. Qiu, Z. L. Yang, C. Wang, Y. Chai, Z. J. Zheng, *Nat. Mater.* **2021**, *20*, 859.
[12] J. Qi, Z. Chen, P. Jiang, W. Hu, Y. Wang, Z. Zhao, X. Cao, S. Zhang, R. Tao, Y. Li, D. Fang, *Adv. Sci.*https://doi.org/10.1002/advs.202102662e2102662.
[13] A. Lendlein, S. Kelch, *Angew. Chem., Int. Ed.* **2002**, *41*, 2034.
[14] Z. Xiang, C. Z. Chu, H. Xie, T. Xiang, S. B. Zhou, *ACS Appl. Mater. Interfaces* **2021**, *13*, 1463.
[15] Z. Zeng, B. Q. Cong, J. P. Oliveira, W. C. Ke, N. Schell, B. Peng, Z. W. Qi, F. G. Ge, W. Zhang, S. S. Ao, *Addit. Manuf.* **2020**, *32*, 10.
[16] R. Xiao, *Int. J. Appl. Mech.* **2016**, *8*, 1640004.
[17] Z. L. Wu, M. Moshe, J. Greener, H. Therien-Aubin, Z. H. Nie, E. Sharon, E. Kumacheva, *Nat. Commun.* **2013**, *4*, 7.
[18] S. B. Choi, C. J. Han, C. R. Lee, J. W. Kim, *Adv. Mater. Technol.* **2020**, *5*, 9.
[19] Y. D. Chi, Y. C. Tang, H. J. Liu, J. Yin, *Adv. Mater. Technol.* **2020**, *5*, 2000370.
[20] D. M. Kochmann, K. Bertoldi, *Appl. Mech. Rev.* **2017**, *69*, 24.
[21] Z. H. Zhou, Y. W. Ni, Z. Z. Tong, S. B. Zhu, J. B. Sun, X. S. Xu, *Int. J. Mech. Sci.* **2019**, *151*, 537.
[22] P. H. Cong, T. M. Chien, N. D. Khoa, N. D. Duc, *Aerosp. Sci. Technol.* **2018**, *77*, 419.
[23] W. J. Zhu, T. Low, V. Perebeinos, A. A. Bol, Y. Zhu, H. G. Yan, J. Tersoff, P. Avouris, *Nano Lett.* **2012**, *12*, 3431.
[24] Z. Ma, S. Li, Y. W. Zheng, M. M. Xiao, H. Jiang, J. H. Gao, X. C. Xie, *Sci. Bull.* **2021**, *66*, 18.
[25] S. Roh, L. B. Okello, N. Golbasi, J. P. Hankwitz, J. A. C. Liu, J. B. Tracy, O. D. Velev, *Adv. Mater. Technol.* **2019**, *4*, 6.
[26] C. J. Cao, X. Gao, A. T. Conn, *Adv. Mater. Technol.* **2019**, *4*, 6.
[27] X. F. Cao, S. H. Xuan, S. S. Sun, Z. B. Xu, J. Li, X. L. Gong, *ACS Appl. Mater. Interfaces* **2021**, *13*, 30127.
[28] L. Ding, J. Y. Zhang, Q. Shu, S. Y. Liu, S. H. Xuan, X. L. Gong, D. S. Zhang, *ACS Appl. Mater. Interfaces* **2021**, *13*, 13724.
[29] M. Ha, G. S. C. Bermudez, J. A. C. Liu, E. S. O. Mata, B. A. Evans, J. B. Tracy, D. Makarov, *Adv. Mater.* **2021**, *33*, 12.
[30] Y. Alapan, A. C. Karacakol, S. N. Guzelhan, I. Isik, M. Sitti, *Sci. Adv.* **2020**, *6*, 9.
[31] W. Q. Hu, G. Z. Lum, M. Mastrangeli, M. Sitti, *Nature* **2018**, *554*, 81.
[32] J. Y. Zhang, H. M. Pang, Y. Wang, X. L. Gong, *Compos. Sci. Technol.* **2020**, *191*, 8.
[33] J. Y. Zhang, Y. Wang, H. M. Pang, S. S. Sun, Z. B. Xu, L. J. Shen, X. F. Cao, C. L. Sun, B. C. Wang, X. L. Gong, *Compos. - A: Appl. Sci. Manuf.* **2021**, *150*, 11.
[34] Y. Kim, G. A. Parada, S. D. Liu, X. H. Zhao, *Sci. Robot.* **2019**, *4*, 15.
[35] R. K. Zhao, Y. Kim, S. A. Chester, P. Sharma, X. H. Zhao, *J. Mech. Phys. Solids* **2019**, *124*, 244.
[36] L. Wang, D. C. Zheng, P. Harker, A. B. Patel, C. F. Guo, X. H. Zhao, *Proc. Natl. Acad. Sci. U. S. A.* **2021**, *118*, 8.
[37] V. K. Venkiteswaran, D. K. Tan, S. Misra, *Extreme Mech. Lett.* **2020**, *41*, 101023.
[38] M. Luo, E. H. Skorina, W. J. Tao, F. C. Chen, S. Ozel, Y. N. Sun, C. D. Onal, *Soft Rob.* **2017**, *4*, 117.
[39] T. Hu, S. H. Xuan, L. Ding, X. L. Gong, *Sens. Actuators, B* **2020**, *314*, 128095.
[40] S. Liu, S. Wang, S. H. Xuan, S. S. Zhang, X. W. Fan, H. Jiang, P. G. Song, X. L. Gong, *ACS Appl. Mater. Interfaces* **2020**, *12*, 15675.
[41] G. S. C. Bermudez, H. Fuchs, L. Bischoff, J. Fassbender, D. Makarov, *Nat. Electron.* **2018**, *1*, 589.
[42] J. W. Chen, Y. T. Zhu, X. H. Chang, D. Pan, G. Song, Z. H. Guo, N. Naik, *Adv. Funct. Mater.* **2021**, *31*, 34.
[43] R. Wang, N. Jiang, J. Su, Q. Yin, Y. Zhang, Z. S. Liu, H. B. Lin, F. A. Moura, N. Y. Yuan, S. Roth, R. S. Rome, R. Ovalle-Robles, K. Inoue, S. G. Yin, S. L. Fang, W. C. Wang, J. N. Ding, L. Q. Shi, R. H. Baughman, Z. F. Liu, *Adv. Funct. Mater.* **2017**, *27*, 13.
[44] T. Kim, M. Kaur, W. S. Kim, *Adv. Mater. Technol.* **2019**, *4*, 8.
[45] W. Liao, Z. Q. Yang, *Adv. Mater. Technol.*https://doi.org/10.1002/admt.2021012609.